DOI: 10.1364/OPTICA.7.000135

Research Article Vol. 7, No. 2 / February 2020 / Optica 135

Visible nonlinear photonics via high-order-mode dispersion engineering

Yun Zhao,[1,*] Xingchen Ji,[1,2] Bok Young Kim,[3] Prathamesh S. Donvalkar,[3,4] Jae K. Jang,[3] Chaitanya Joshi,[3,4] Mengjie Yu,[2,3] Chaitali Joshi,[3,4] Renato R. Domeneguetti,[5] Felippe A. S. Barbosa,[1] Paulo Nussenzveig,[5] Yoshitomo Okawachi,[3] Michal Lipson,[1,3] and Alexander L. Gaeta[1,3]

[1]Department of Electrical Engineering, Columbia University, New York, New York 10027, USA
[2]School of Electrical and Computer Engineering, Cornell University, Ithaca, New York 14853, USA
[3]Department of Applied Physics and Applied Mathematics, Columbia University, New York, New York 10027, USA
[4]School of Applied and Engineering Physics, Cornell University, Ithaca, New York 14853, USA
[5]Instituto de Fisica, Universidade de São Paulo, P.O. Box 66318, São Paulo 05315-970, Brazil
*Corresponding author: yz3019@columbia.edu

Received 26 August 2019; revised 16 October 2019; accepted 21 October 2019 (Doc. ID 376156); published 29 January 2020

Over the past decade, remarkable advances have been realized in chip-based nonlinear photonic devices for classical and quantum applications in the near- and mid-infrared regimes. However, few demonstrations have been realized in the visible and near-visible regimes, primarily due to the large normal material group-velocity dispersion (GVD) that makes it challenging to phase match third-order parametric processes. In this paper, we show that exploiting dispersion engineering of higher-order waveguide modes provides waveguide dispersion that allows for small or anomalous GVD in the visible and near-visible regimes and phase matching of four-wave mixing processes. We illustrate the power of this concept by demonstrating in silicon nitride microresonators a near-visible mode-locked Kerr frequency comb and a narrowband photon-pair source compatible with Rb transitions. These realizations extend applications of nonlinear photonics towards the visible and near-visible regimes for applications in time and frequency metrology, spectral calibration, quantum information, and biomedical applications.

https://doi.org/10.1364/OPTICA.7.000135

1. INTRODUCTION

With the rapid development of nanofabrication techniques, nonlinear- and quantum-based applications are being realized in chip-scale devices. In order to operate with high efficiency, third-order parametric nonlinear processes must satisfy phase-matching (PM) conditions largely governed by the group-velocity dispersion (GVD). In photonic waveguides, the GVD has contributions from the material and from the waveguide confinement. The waveguide GVD can be tuned by changing the structure dimensions [1], which for four-wave mixing requires anomalous or near-zero GVD. This is critical for applications such as Kerr frequency comb generation (KCG) [2,3] and photon-pair generation (PPG) [4]. For all photonic materials [e.g., silicon nitride (SiN), silica, etc.] the GVD becomes highly normal at shorter wavelengths, which makes it impossible to satisfy the PM conditions with conventional waveguide dispersion engineering. Overcoming this obstacle is essential to developing chip-based photonics in the visible and near-visible regimes.

In this paper, we perform dispersion engineering by utilizing the high-order-modes of chip-based waveguides to create anomalous GVD across a large range of wavelengths in the near-visible and visible regimes. We demonstrate the power of this dispersion engineering by generating broadband Kerr combs near 784 nm, which represents the first soliton comb at this wavelength regime using a monolithically integrated chip-based platform. The low wavelength side of the comb reaches visible regime (<740 nm; the definition of visible regime may vary), which are the shortest wavelength components generated directly by a Kerr frequency comb. We also show that this dispersion engineering enables a silicon chip-based narrowband photon-pair source at near-visible wavelengths and is compatible with rubidium (Rb) quantum memories (operating near 795 nm). We also show through simulation that combs deep in the visible are possible, which overlap Hg^+ and Yb transitions.

2. DISPERSION ENGINEERING USING HIGH-ORDER MODES

The refractive indices of most materials can be modeled by a simple two-level system [5], which yields the Sellmeier equation. Such a model yields a refractive index $n(\omega)$ that scales as $(\omega_0^2 - \omega^2)^{-1/2}$, where ω_0 is the frequency of the material resonance. For visible light, the dominating resonance frequency

Corrected 29 January 2020

corresponds to the bandgap energy, which creates strong normal GVD as the light frequency shifts towards it.

To illustrate the power of dispersion engineering using high-order waveguide modes, we start with normalized parameters [6] for a step-index slab waveguide [inset, Fig. 1(a)]. Our results capture the behavior of rectangular waveguides since their effective refractive index can be approximated by two slab waveguides with the effective index method [6]. The two essential parameters are

$$V = \frac{\omega}{c} h \sqrt{n_{co}^2 - n_{cl}^2}, \tag{1}$$

$$b \approx \frac{2 n_{co} n_{eff}}{n_{co}^2 - n_{cl}^2}, \tag{2}$$

where V, b are the normalized frequency and refractive index, respectively, c is the speed of light, h is the waveguide height, and n_{co} and n_{cl} are the refractive indices of the core and the cladding, respectively. For TE modes, V and b obey the transcendental equation

$$V\sqrt{1-b} = m\pi + 2\tan^{-1}\sqrt{b/(1-b)}, \tag{3}$$

where m is the mode order. Equation (3) is useful in analyzing the dispersion properties of waveguides [7], and we focus our attention on the waveguide dispersion by setting the material dispersion to zero, that is, n_{co} and n_{cl} are independent of ω. The waveguide GVD can then be written as

$$\beta_{2,wg} = (n_{co}^2 - n_{cl}^2)^{\frac{3}{2}} \frac{h}{2 n_{co} c^2} B_2(V), \tag{4}$$

where $B_2(V) = \frac{d^2(Vb)}{dV^2}$ is the normalized GVD and contains the general waveguide GVD properties. Due to the transcendental nature of Eq. (3), B_2 is calculated numerically. From Fig. 1(a), we observe that close to the cutoff frequency, B_2 is strongly positive (normal). As the frequency increases, B_2 becomes strongly negative (anomalous) and then gradually decreases in magnitude while maintaining its sign. More importantly, we find that the higher-order modes can produce larger negative B_2 than the lower-order ones. A similar idea is shown for whispering gallery mode resonators (WGMRs), where the analysis takes a different approach [8].

Designing a waveguide that compensates for the large normal GVD of photonic materials in the near-visible and visible regimes requires access to the large negative part of B_2. This can be achieved by using high-order modes and small waveguide structures. In this work, we base our devices on the SiN platform. We use a finite-element method (FEM) mode solver with a well characterized Sellmeier equation for our SiN thin film [9] to accurately model the total GVD of rectangular waveguides and microresonators. Although stronger anomalous GVD can be realized with a smaller waveguide size, the reduction in size also introduces additional losses due to an increase in scattering at the core–cladding interface. For the current experiments, we choose a waveguide cross section of 730 nm × 1330 nm and a ring resonator radius of 22 μm, with a width fabrication uncertainty of ±40 nm. The simulated GVD is plotted in Fig. 1(b). We operate at the TE_{10} mode, whose zero-GVD point is near 760 nm. We design the bus-ring coupling region so that the TE_{00} mode of the bus excites the TE_{10} mode of the ring [10]. This is done by matching the effective refractive index of the two modes, which leads to bus dimensions of 730 × 568 nm [Fig. 1(c)]. In this way, we ensure that the input and output modes are fundamental even though the resonating modes are in higher order, making this device easy to interface with any other on-chip component. To verify that the TE_{10} mode is indeed excited, in selected devices we include a drop port that has the same cross section as the ring. The mode profile in the ring can be imaged at the output of the drop port [top inset, Fig. 1(d)] with a microscope configuration

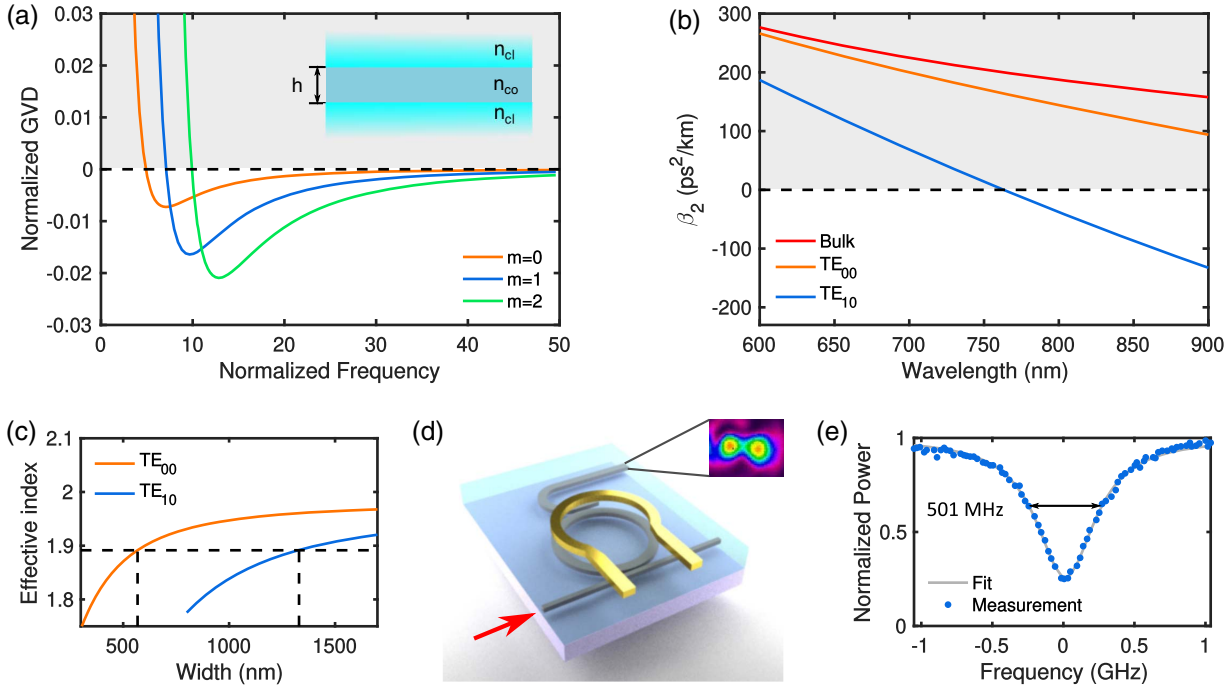

Fig. 1. (a) Normalized GVD. Inset, structure of the slab waveguide. (b) Simulated GVD for a 730 × 1330 nm microring resonator with a bending radius of 22 μm. (c) Effective refractive index of the TE_{00} mode of a straight waveguide and TE_{10} mode of a ring. Efficient mode conversion is realized when the two modes have the same effective indices. (d) Device schematic. Inset, measured mode profile. (e) Measured resonance.

and a camera. These drop-port devices, however, are not used for KCG or PPG, since the extra coupling loss reduces the Q. The final schematic of the device is shown in Fig. 1(d). We characterize the Q of our devices using a wavemeter-calibrated frequency scan and a Lorentzian fit. The full width at half-maximum (FWHM) is measured to be 501 MHz, which corresponds to a loaded Q of 7.7×10^5 with an extinction ratio of 74%.

3. KERR COMB GENERATION

The first application we demonstrate using this high-order-mode nonlinear microresonator is KCG reaching the visible regime. Kerr frequency combs provide a pathway towards fully integrated comb sources that could find applications across numerous areas of science and engineering [2,3,11,12], including spectroscopy [13–16], ranging [17,18], frequency synthesizers [19], and coherent communication [20]. Moreover, extending KCG to near-visible and visible wavelengths enables additional applications in optical clockwork [21,22], astronomical spectrograph calibration [23–25], and biological imaging [26,27]. Additionally, these wavelength regimes are compatible with low-cost high-quality Si-based detectors and cameras. Various schemes have been proposed and tested in the past, including direct generation [28–31] and frequency conversion from telecom combs [32,33], but to date, mode-locking has only been demonstrated by Lee *et al.* [34] near 778 nm using a silica WGMR. While SiN has proven to be highly promising platform in the near-IR, at near-visible wavelengths, SiN has a material GVD that is more than 5 times higher than that of the silica used in [34]. To date, the lowest wavelength achieved by a mode-locked Kerr comb on this platform is demonstrated by Yu *et al.* near 770 nm [35] by generating a dispersive wave fed by a main soliton pumped at 1 μm. The dispersive wave process is governed by the higher-order dispersion coefficients, making it highly sensitive to fabrication variations [36]. It is thus advantageous to generate a soliton centered in this wavelength regime, since it also can provide higher comb power as compared to dispersive waves.

We generate a soliton mode-locked comb using the device described in the previous section with the thermal tuning method as demonstrated by Joshi *et al.* [37]. Specifically, we fix the pump laser frequency to the blue side of the resonance and decrease the heater voltage, which blue-detunes the resonance. At the output, we record the comb spectrum and power. The output power curve [Fig. 2(b)] is composed of four segments that correspond to four different dynamical processes leading to the final mode-locked comb, namely, subthreshold state, Turing pattern state, chaotic state, and soliton state. The heater voltage is slightly increased after the transition into soliton state (known as the "soliton step") to compensate for the temperature difference owing to an abrupt change of intracavity power. In Fig. 2(c), we show the spectrum of a four-soliton state where the solitons are equally spaced inside the ring [inset, Fig. 2(c)]. This is the preferred state, since it has an intracavity power that is close to that of the chaotic state, making it experience the least amount of thermal backlash after the soliton step, which we find to be more pronounced than

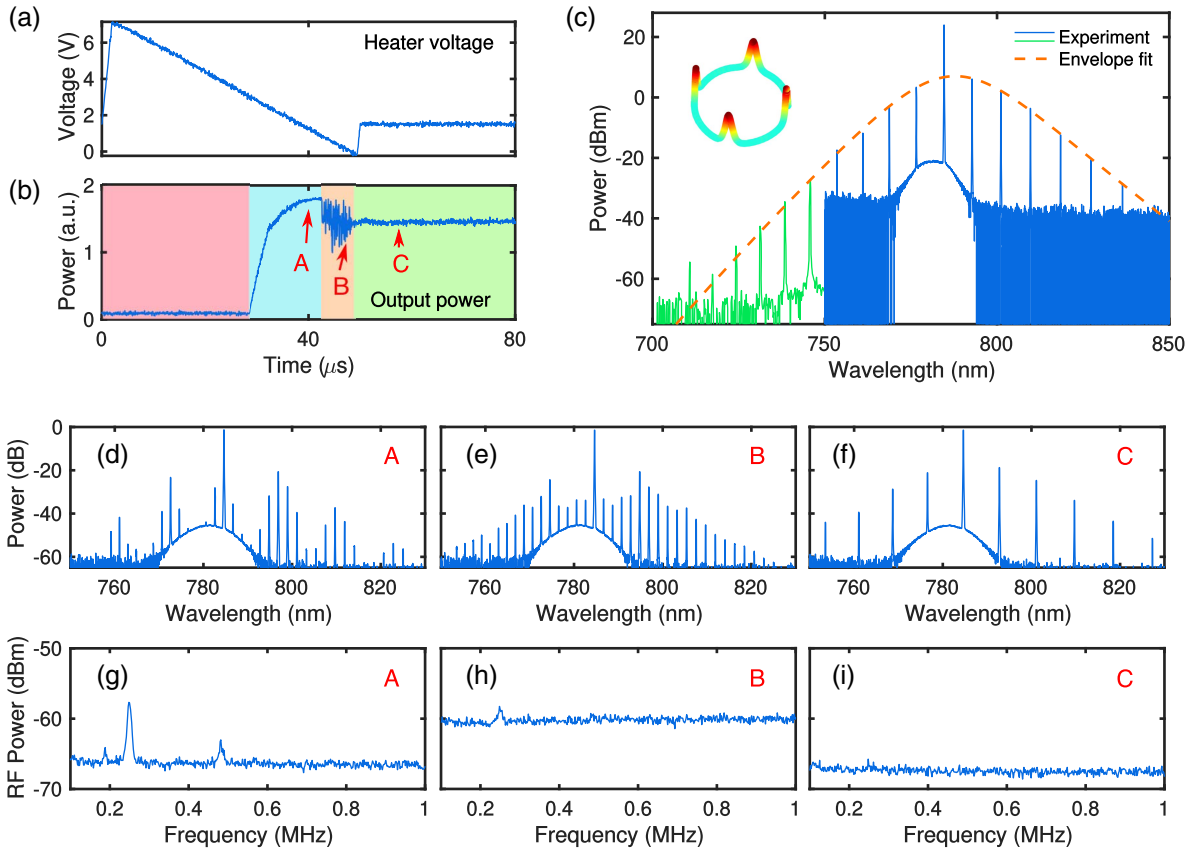

Fig. 2. (a) Voltage pattern used to modulate the on-chip heater. (b) Evolution of comb power corresponding to the pattern in (a). (c) Experimental comb spectrum calibrated for collection losses. Inset, simulated intracavity four-soliton state. (d–f) Optical spectra corresponding to point A (minicomb formation), B (chaotic state), and C (soliton state) in (b), respectively. (g–i) RF noise corresponding to (d)–(f).

in the near-IR. For pumping at 782 nm, which is one free spectral range (FSR) away from 784 nm, the five-soliton state is found to be most stable, indicating that a mode interaction near 792 nm is the dominant factor in determining the pattern of the soliton state [38]. Limited by the dynamic range of the optical spectrum analyzer (≈60 dB), we obtain the spectrum in two shots under the same experimental conditions. We observe comb lines down to 710 nm, which represents the shortest wavelength generated by a mode-locked Kerr comb. We then fit our experiment spectrum with a sech^2 envelope which yields a 3 dB bandwidth of 9.9 THz.

We further characterize the noise properties of the generated soliton state with a radio-frequency spectrum analyzer (RFSA). We gradually tune the pump laser into resonance and record the noise at three different stages of the KCG process [indicated in Fig. 2(b)], namely, the (A) minicomb state, (B) chaotic state, and (C) soliton state. As observed previously [37], the minicomb stage has a low noise floor with sharp peaks, the chaotic state has broadband and high noise, and the soliton state has a flat noise spectrum and the lowest RF noise of all three stages.

One appealing property of the generated near-visible combs is that they span several atomic transitions that are commonly used for time and frequency metrology. For example, the transitions allow for full stabilization of the comb by locking two of the comb lines to two atomic transitions [22]. Here, we show the interaction between our comb and Rb atoms by scanning a comb line near 795 nm across the well-known Rb D1 transition. To generate such a comb line from our four-soliton state, we increase our pump power from 220 to 270 mW. At large pump-cavity detuning, we observe weaker comb lines appearing between the strong comb lines [Fig. 3(a)]. This is caused by the disruption of the perfect symmetric soliton locations due to high power, which is well modeled in our simulations [Fig. 3(b)]. We use a bandpass filter to select the comb line near 795 nm and send it through a 2 cm-long ^{85}Rb pure isotope cell held at 53.7°C. As a result of soft thermal locking [39], this comb line can be tuned by up to 10 GHz by simply tuning the pump wavelength. In our experiment, we tune the pump laser by 5 GHz through piezoelectric tuning and record the transmission of the 795-nm comb line [Fig. 3(c)]. We also fit our experimental data to the theoretical calculations based on published properties of Rb [40]. The fitting parameters are the atomic density, the location of the zero detuning (defined by the $F = 3$ to $F' = 2$ transition), and the scanning range. We observe good agreement between theory and experiment, indicating that the comb lines are strongly interacting with atoms. The slightly lower transmission at the two extremes of detuning is caused by residual ^{85}Rb atoms in the ^{85}Rb cell.

4. PHOTON-PAIR GENERATION

Nonlinear photonic devices in the near-visible and visible wavelength regime are important for quantum applications. First, nonclassical states can only be generated through nonlinear processes. Secondly, the existence of high-quality avalanche photodetectors (APDs) and well-studied atomic transitions at this wavelength regime makes it extremely attractive. As an example of near-visible quantum optics in our high-order-mode nonlinear microresonator, we show correlated narrowband PPG in this wavelength regime, which has important application in Rb or cesium memory-based quantum information networks [41–43]. Previously, such photon pairs have been generated via spontaneous four-wave mixing (SFWM) in warm alkali vapor [44] or via spontaneous parametric downconversion (SPDC) in a bulk lithium niobate WGMR [45] and a lithium niobate Fabry–Perot cavity [46]. PPG in SiN microresonators is promising for quantum information applications due to its scalability and low loss [47]. Moreover, the flexibility in nanofabrication provides ways for better controlling of the photon states [48–50]. Lu *et al.* [51] demonstrated the correlation between one visible and one telecom photon generated from a SiN microresonator [35]. However, for applications that do not require long-distance fiber communication, such as free-space quantum communication and memory-assisted quantum computing [52], it is desirable to generate both photons at near-visible wavelengths, which has lower design and fabrication complexity. Moreover, due to their similarity, both photons can be further manipulated with the same devices and be detected with room-temperature high-efficiency silicon-based APDs.

We generate near-visible photon pairs by driving our microresonator at pump powers below the parametric oscillation threshold. We set our pump at 784.7 nm and use bandpass filters to select photons at 794.8 nm (signal) and 774.9 nm (idler). We verify the photon correlation by measuring the coincidence function $g^{(2)}_{si}(\tau)$ between the signal and idler. We observe a clear coincidence peak at zero relative delay [Fig. 4(a)]. We also observe a significant amount of uncorrelated noise photons, which is proportional to the pump power in the bus waveguide (see Supplement 1). This is due to SiN used in our samples being slightly Si-rich, which generates broadband fluorescence when pumped below 1.1 μm. This can be overcome by refining the fabrication process to reduce the Si concentration [53]. Since

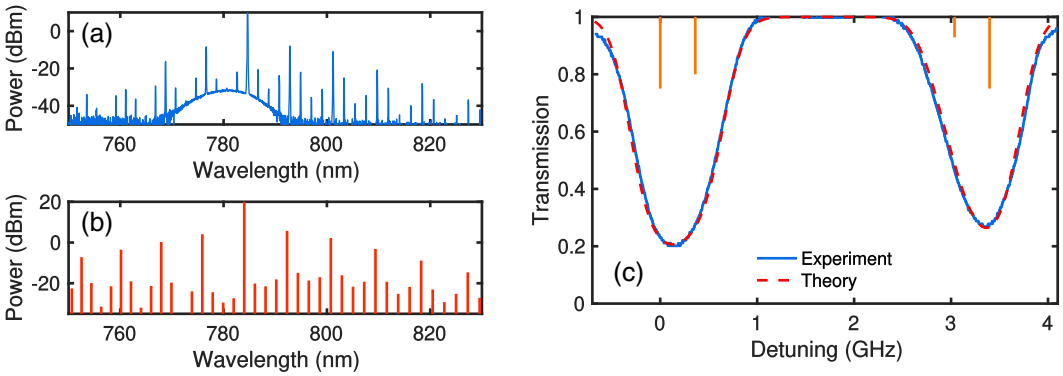

Fig. 3. (a) Asymmetric four-soliton state with denser comb line spacing. (b) Simulated spectrum of (a). (c) Rb D1 transition probed by a comb line of our near-visible comb. The Doppler-free transitions and their relative strengths are shown as vertical sticks.

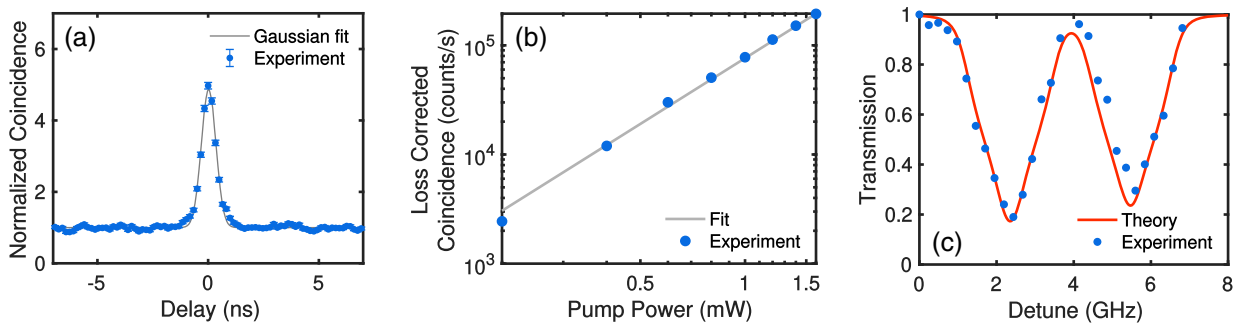

Fig. 4. (a) Normalized coincidence between signal and idler $g_{si}^{(2)}(\tau)$. (b) PPG rate scaling. The plot is corrected for collection and detector losses. (c) Photon interaction with Rb D1 transition.

the FWHM of each resonance is 501 MHz, the theoretical FWHM of $g_{si}^{(2)}$ is 238 ps [54], which is comparable to the timing jitter of our single-photon counting module (SPCM), and thus cannot be readily resolved in our $g_{si}^{(2)}(\tau)$ measurement. We further characterize the generation rate by measuring the coincidence at different pump power levels. The generation rate is proportional to the square of the pump power, as all data points fall on a straight line with a slope of 2 in the log–log plot [Fig. 4(b)]. We fit the measurement and achieve a PPG efficiency of 7.6×10^4 pairs s^{-1} mW^{-2} for these narrowband photons, which is comparable to many other cavity-enhanced PPG demonstrations [55].

Our photon source is also easily tunable by jointly controlling the pump wavelength and the on-chip heater. We show the tunability by sending the signal through an Rb vapor cell and tuning it across the D1 transition. Figure 4(c) shows the normalized coincidence rate versus the pump detuning. For stable operation, we blue-detune the pump to operate in the soft thermal locking regime [39]. Since this is comparable to the FWHM bandwidth of the resonance, it must be incorporated into the photon model. The photon spectrum has the shape

$$S(\omega) \propto \frac{1}{(4\omega^2 + \Delta\omega^2 - \mathcal{W})^2 + 4\Delta\omega^2\mathcal{W}}, \tag{5}$$

where ω is the frequency detuning, $\Delta\omega$ is the FWHM angular frequency of the resonance, and $\mathcal{W}$ (which can assume both signs) is the combined effect of the pump detuning, dispersion, and cross phase modulation (see Supplement 1). The theoretical curve is calculated by first measuring the Rb atomic density of the cell separately with a laser and the photon wavelength with a wavemeter by driving the ring above threshold. The theoretical transmission versus detuning curve is a convolution of the Rb absorption spectrum and the photon spectrum in Eq. (5). We also notice that a cavity mode interaction is present at the signal resonance, which effectively increases the pump detuning (see Supplement 1). We leave the pump detuning as the only free parameter to fit the measurement. There are ±1°C temperature fluctuations and constant air turbulence near the cell due to the heating. Nonetheless, the good agreement between experiment and theory indicates that the properties of photons are well characterized.

5. DISCUSSION

We can take advantage of higher-order mode dispersion engineering for KCG at even shorter wavelengths. The state-of-the-art mode-locked Ti:sapphire oscillator has been shown to produce spectral components below 600 nm [56], enabling the interaction with more species of clock atoms. Our simulations show that this can also be achieved by higher-order mode Kerr combs with realistic parameters. Following the previous argument, a tighter mode confinement is required to push the anomalous GVD region to shorter wavelengths. In Fig. 5(a), we show FEM simulation of a 400 nm × 1000 nm SiN waveguide cladded by SiO_2, with a bending radius of 100 μm. The TE_{20} mode has a zero GVD point at 587 nm. We simulate the corresponding soliton spectrum using the Lugiato–Lefever equation [57], where we assume a pump of 300 mW at 595 nm and a resonance FWHM of 700 MHz [Fig. 5(b)]. We see the clock transitions of Hg^+ (563 nm) and Yb (578 nm) atoms are covered by sufficiently strong comb lines [58]. While anomalous GVD can be achieved at even shorter wavelengths with even higher-order modes, the increased cavity losses caused by the use of these modes at shorter wavelengths, as well as the onset of two-photon absorption, pose significant challenges to Kerr comb generation below 550 nm via this approach.

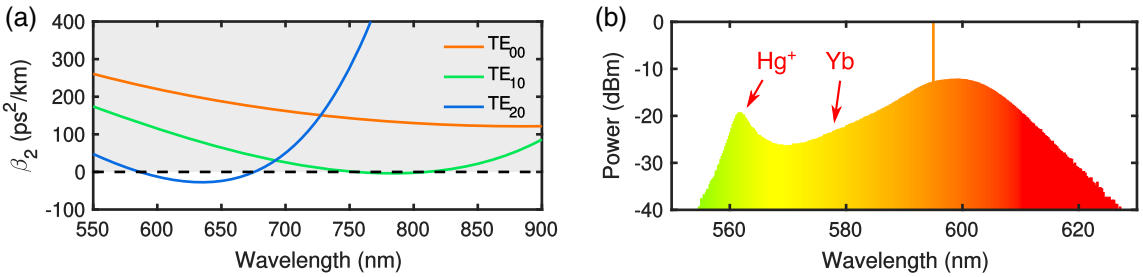

Fig. 5. (a) Simulated dispersion of a microresonantor with 400 nm × 1000 nm cross section and 100 μm bending radius. (b) Simulated Kerr comb spectrum for the TE_{20} mode in (a).

Even though in principle PPG can occur regardless of PM, in practice PM is required to achieve a high generation rate and to avoid spurious processes. In our model for PPG with dispersion (see Supplement 1), we also find that PM contributes to the narrowness of the photon bandwidth. Notably, a blue-detuned pump balances the phase mismatch that comes from a small anomalous GVD so that both high generation rate and narrow bandwidth can be achieved in this regime.

6. CONCLUSION

In conclusion, we have shown that dispersion engineering through high-order waveguide modes can compensate for the strong normal material GVD at near-visible and visible wavelengths to realize small or anomalous GVD that is not possible with the fundamental modes. With this approach, we designed a high-order-mode nonlinear microresonator that generated the first Kerr comb from a near-visible pump on a monolithically integrated chip-based platform. This dispersion engineering capability enables potential applications such as compact atomic clocks, astrocombs, and high-quality bioimaging light sources. In addition, we used the same nonlinear microresonator to demonstrate, to the best of our knowledge, the first silicon-chip-based narrowband near-visible photon-pair source that could enable applications in memory-based quantum information networks.

Funding. Air Force Office of Scientific Research (FA9550-15-1-0303); National Science Foundation (EFMA-1641094, PHY-1707918).

Acknowledgment. The authors thank Dr. Alessandro Farsi, Dr. Sven Ramelow, and Dr. Aseema Mohanty for helpful discussions.

Please see Supplement 1 for supporting content.

REFERENCES

1. A. C. Turner, C. Manolatou, B. S. Schmidt, M. Lipson, M. A. Foster, J. E. Sharping, and A. L. Gaeta, "Tailored anomalous group-velocity dispersion in silicon channel waveguides," Opt. Express **14**, 4357–4362 (2006).
2. T. J. Kippenberg, A. L. Gaeta, M. Lipson, and M. L. Gorodetsky, "Dissipative Kerr solitons in optical microresonators," Science **361**, eaan8083 (2018).
3. A. L. Gaeta, M. Lipson, and T. J. Kippenberg, "Photonic-chip-based frequency combs," Nat. Photonics **13**, 158–169 (2019).
4. M. Kues, C. Reimer, J. M. Lukens, W. J. Munro, A. M. Weiner, D. J. Moss, and R. Morandotti, "Quantum optical microcombs," Nat. Photonics **13**, 170–179 (2019).
5. R. W. Boyd, *Nonlinear Optics*, 3rd ed. (Academic, 2008).
6. C. R. Pollock and M. Lipson, *Integrated Photonics* (Kluwer Academic, 2003).
7. G. A. Bennett and C.-L. Chen, "Wavelength dispersion of optical waveguides," Appl. Opt. **19**, 1990–1995 (1980).
8. A. A. Savchenkov, A. B. Matsko, W. Liang, V. S. Ilchenko, D. Seidel, and L. Maleki, "Kerr combs with selectable central frequency," Nat. Photonics **5**, 293–296 (2011).
9. K. Luke, Y. Okawachi, M. R. E. Lamont, A. L. Gaeta, and M. Lipson, "Broadband mid-infrared frequency comb generation in a Si_3N_4 microresonator," Opt. Lett. **40**, 4823–4826 (2015).
10. L.-W. Luo, N. Ophir, C. P. Chen, L. H. Gabrielli, C. B. Poitras, K. Bergmen, and M. Lipson, "WDM-compatible mode-division multiplexing on a silicon chip," Nat. Commun. **5**, 3069 (2014).
11. T. Herr, V. Brasch, J. D. Jost, C. Y. Wang, N. M. Kondratiev, M. L. Gorodetsky, and T. J. Kippenberg, "Temporal solitons in optical microresonators," Nat. Photonics **8**, 145–152 (2014).
12. B. Stern, X. Ji, Y. Okawachi, A. L. Gaeta, and M. Lipson, "Battery-operated integrated frequency comb generator," Nature **562**, 401–405 (2018).
13. M.-G. Suh, Q.-F. Yang, K. Y. Yang, X. Yi, and K. J. Vahala, "Microresonator soliton dual-comb spectroscopy," Science **354**, 600–603 (2016).
14. N. G. Pavlov, G. Lihachev, S. Koptyaev, E. Lucas, M. Karpov, N. M. Kondratiev, I. A. Bilenko, T. J. Kippenberg, and M. L. Gorodetsky, "Soliton dual frequency combs in crystalline microresonators," Opt. Lett. **42**, 514–517 (2017).
15. M. Yu, Y. Okawachi, A. G. Griffith, N. Picqué, M. Lipson, and A. L. Gaeta, "Silicon-chip-based mid-infrared dual-comb spectroscopy," Nat. Commun. **9**, 1869 (2018).
16. A. Dutt, C. Joshi, X. Ji, J. Cardenas, Y. Okawachi, K. Luke, A. L. Gaeta, and M. Lipson, "On-chip dual-comb source for spectroscopy," Sci. Adv. **4**, e1701858 (2018).
17. P. Trocha, M. Karpov, D. Ganin, M. H. P. Pfeiffer, A. Kordts, S. Wolf, J. Krockenberger, P. Marin-Palomo, C. Weimann, S. Randel, W. Freude, T. J. Kippenberg, and C. Koos, "Ultrafast optical ranging using microresonator soliton frequency combs," Science **359**, 887–891 (2018).
18. M.-G. Suh and K. J. Vahala, "Soliton microcomb range measurement," Science **359**, 884–887 (2018).
19. D. T. Spencer, T. Drake, T. C. Briles, J. Stone, L. C. Sinclair, C. Fredrick, Q. Li, D. Westly, B. R. Ilic, A. Bluestone, N. Volet, T. Komljenovic, L. Chang, S. H. Lee, D. Y. Oh, M.-G. Suh, K. Y. Yang, M. H. P. Pfeiffer, T. J. Kippenberg, E. Norberg, L. Theogarajan, K. Vahala, N. R. Newbury, K. Srinivasan, J. E. Bowers, S. A. Diddams, and S. B. Papp, "An optical-frequency synthesizer using integrated photonics," Nature **557**, 81–85 (2018).
20. P. Marin-Palomo, J. N. Kemal, M. Karpov, A. Kordts, J. Pfeifle, M. H. P. Pfeiffer, P. Trocha, S. Wolf, V. Brasch, M. H. Anderson, R. Rosenberger, K. Vijayan, W. Freude, T. J. Kippenberg, and C. Koos, "Microresonator-based solitons for massively parallel coherent optical communications," Nature **546**, 274–279 (2017).
21. J. Vanier, "Atomic clocks based on coherent population trapping: a review," Appl. Phys. B **81**, 421–442 (2005).
22. S. B. Papp, K. Beha, P. Del'Haye, F. Quinlan, H. Lee, K. J. Vahala, and S. A. Diddams, "Microresonator frequency comb optical clock," Optica **1**, 10–14 (2014).
23. C.-H. Li, A. J. Benedick, P. Fendel, A. G. Glenday, F. X. Kärtner, D. F. Phillips, D. Sasselov, A. Szentgyorgyi, and R. L. Walsworth, "A laser frequency comb that enables radial velocity measurements with a precision of 1 cm s^{-1}," Nature **452**, 610–612 (2008).
24. E. Obrzud, M. Rainer, A. Harutyunyan, M. H. Anderson, J. Liu, M. Geiselmann, B. Chazelas, S. Kundermann, S. Lecomte, M. Cecconi, A. Ghedina, E. Molinari, F. Pepe, F. Wildi, F. Bouchy, T. J. Kippenberg, and T. Herr, "A microphotonic astrocomb," Nat. Photonics **13**, 31–35 (2019).
25. M.-G. Suh, X. Yi, Y.-H. Lai, S. Leifer, I. S. Grudinin, G. Vasisht, E. C. Martin, M. P. Fitzgerald, G. Doppmann, J. Wang, D. Mawet, S. B. Papp, S. A. Diddams, C. Beichman, and K. Vahala, "Searching for exoplanets using a microresonator astrocomb," Nat. Photonics **13**, 25–30 (2019).
26. S.-J. Lee, B. Widiyatmoko, M. Kourogi, and M. Ohtsu, "Ultrahigh scanning speed optical coherence tomography using optical frequency comb generators," Jpn. J. Appl. Phys. **40**, L878 (2001).
27. A. F. Fercher, W. Drexler, C. K. Hitzenberger, and T. Lasser, "Optical coherence tomography: principles and applications," Rep. Prog. Phys. **66**, 239 (2003).
28. K. Saha, Y. Okawachi, J. S. Levy, R. K. W. Lau, K. Luke, M. A. Foster, M. Lipson, and A. L. Gaeta, "Broadband parametric frequency comb generation with a 1-μm pump source," Opt. Express **20**, 26935–26941 (2012).
29. Y. Yang, X. Jiang, S. Kasumie, G. Zhao, L. Xu, J. M. Ward, L. Yang, and S. N. Chormaic, "Four-wave mixing parametric oscillation and frequency comb generation at visible wavelengths in a silica microbubble resonator," Opt. Lett. **41**, 5266–5269 (2016).
30. L. Wang, L. Chang, N. Volet, M. H. P. Pfeiffer, M. Zervas, H. Guo, T. J. Kippenberg, and J. E. Bowers, "Frequency comb generation in the green using silicon nitride microresonators," Laser Photon. Rev. **10**, 631–638 (2016).

31. M. Soltani, A. Matsko, and L. Maleki, "Enabling arbitrary wavelength frequency combs on chip," Laser Photon. Rev. **10**, 158–162 (2016).
32. S. Miller, K. Luke, Y. Okawachi, J. Cardenas, A. L. Gaeta, and M. Lipson, "On-chip frequency comb generation at visible wavelengths via simultaneous second- and third-order optical nonlinearities," Opt. Express **22**, 26517–26525 (2014).
33. X. Guo, C.-L. Zou, H. Jung, Z. Gong, A. Bruch, L. Jiang, and H. X. Tang, "Efficient generation of a near-visible frequency comb via Cherenkov-like radiation from a Kerr microcomb," Phys. Rev. Appl. **10**, 014012 (2018).
34. S. H. Lee, D. Y. Oh, Q.-F. Yang, B. Shen, H. Wang, K. Y. Yang, Y.-H. Lai, X. Yi, X. Li, and K. Vahala, "Towards visible soliton microcomb generation," Nat. Commun. **8**, 1295 (2017).
35. S.-P. Yu, T. C. Briles, G. T. Moille, X. Lu, S. A. Diddams, K. Srinivasan, and S. B. Papp, "Tuning Kerr-soliton frequency combs to atomic resonances," Phys. Rev. Appl. **11**, 044017 (2019).
36. M. H. P. Pfeiffer, C. Herkommer, J. Liu, H. Guo, M. Karpov, E. Lucas, M. Zervas, and T. J. Kippenberg, "Octave-spanning dissipative Kerr soliton frequency combs in Si_3N_4 microresonators," Optica **4**, 684–691 (2017).
37. C. Joshi, J. K. Jang, K. Luke, X. Ji, S. A. Miller, A. Klenner, Y. Okawachi, M. Lipson, and A. L. Gaeta, "Thermally controlled comb generation and soliton modelocking in microresonators," Opt. Lett. **41**, 2565–2568 (2016).
38. D. C. Cole, E. S. Lamb, P. Del'Haye, S. A. Diddams, and S. B. Papp, "Soliton crystals in Kerr resonators," Nat. Photonics **11**, 671–676 (2017).
39. T. Carmon, L. Yang, and K. J. Vahala, "Dynamical thermal behavior and thermal self-stability of microcavities," Opt. Express **12**, 4742–4750 (2004).
40. P. Siddons, C. S. Adams, C. Ge, and I. G. Hughes, "Absolute absorption on rubidium D lines: comparison between theory and experiment," J. Phys. B **41**, 155004 (2008).
41. C. Liu, Z. Dutton, C. H. Behroozi, and L. V. Hau, "Observation of coherent optical information storage in an atomic medium using halted light pulses," Nature **409**, 490–493 (2001).
42. D. F. Phillips, A. Fleischhauer, A. Mair, R. L. Walsworth, and M. D. Lukin, "Storage of light in atomic vapor," Phys. Rev. Lett. **86**, 783–786 (2001).
43. T. Chanelière, D. N. Matsukevich, S. D. Jenkins, S.-Y. Lan, T. A. B. Kennedy, and A. Kuzmich, "Storage and retrieval of single photons transmitted between remote quantum memories," Nature **438**, 833–836 (2005).
44. V. Balić, D. A. Braje, P. Kolchin, G. Y. Yin, and S. E. Harris, "Generation of paired photons with controllable waveforms," Phys. Rev. Lett. **94**, 183601 (2005).
45. M. Förtsch, J. U. Fürst, C. Wittmann, D. Strekalov, A. Aiello, M. V. Chekhova, C. Silberhorn, G. Leuchs, and C. Marquardt, "A versatile source of single photons for quantum information processing," Nat. Commun. **4**, 1818 (2013).
46. K.-H. Luo, H. Herrmann, S. Krapick, B. Brecht, R. Ricken, V. Quiring, H. Suche, W. Sohler, and C. Silberhorn, "Direct generation of genuine single-longitudinal-mode narrowband photon pairs," New J. Phys. **17**, 073039 (2015).
47. S. Ramelow, A. Farsi, S. Clemmen, D. Orquiza, K. Luke, M. Lipson, and A. L. Gaeta, "Silicon-nitride platform for narrowband entangled photon generation," arXiv:1508.04358 (2015).
48. J. He, B. A. Bell, A. Casas-Bedoya, Y. Zhang, A. S. Clark, C. Xiong, and B. J. Eggleton, "Ultracompact quantum splitter of degenerate photon pairs," Optica **2**, 779–782 (2015).
49. Z. Vernon, M. Liscidini, and J. E. Sipe, "No free lunch: the trade-off between heralding rate and efficiency in microresonator-based heralded single photon sources," Opt. Lett. **41**, 788–791 (2016).
50. J. B. Christensen, J. G. Koefoed, K. Rottwitt, and C. J. McKinstrie, "Engineering spectrally unentangled photon pairs from nonlinear microring resonators by pump manipulation," Opt. Lett. **43**, 859–862 (2018).
51. X. Lu, Q. Li, D. A. Westly, G. Moille, A. Singh, V. Anant, and K. Srinivasan, "Chip-integrated visible-telecom entangled photon pair source for quantum communication," Nat. Phys. **15**, 373–381 (2019).
52. P. Kok, W. J. Munro, K. Nemoto, T. C. Ralph, J. P. Dowling, and G. J. Milburn, "Linear optical quantum computing with photonic qubits," Rev. Mod. Phys. **79**, 135–174 (2007).
53. J. Smith, J. Monroy-Ruz, J. G. Rarity, and K. C. Balram, "Single photon emission and single spin coherence of a nitrogen vacancy centre encapsulated in silicon nitride," arXiv:1909.09383 (2019).
54. Z. Y. Ou and Y. J. Lu, "Cavity enhanced spontaneous parametric down-conversion for the prolongation of correlation time between conjugate photons," Phys. Rev. Lett. **83**, 2556–2559 (1999).
55. S. Clemmen, K. P. Huy, W. Bogaerts, R. G. Baets, P. Emplit, and S. Massar, "Continuous wave photon pair generation in silicon-on-insulator waveguides and ring resonators," Opt. Express **17**, 16558–16570 (2009).
56. R. Ell, U. Morgner, F. X. Kärtner, J. G. Fujimoto, E. P. Ippen, V. Scheuer, G. Angelow, T. Tschudi, M. J. Lederer, A. Boiko, and B. Luther-Davies, "Generation of 5-fs pulses and octave-spanning spectra directly from a Ti:sapphire laser," Opt. Lett. **26**, 373–375 (2001).
57. S. Coen, H. G. Randle, T. Sylvestre, and M. Erkintalo, "Modeling of octave-spanning Kerr frequency combs using a generalized mean-field Lugiato–Lefever model," Opt. Lett. **38**, 37–39 (2013).
58. T. M. Fortier, A. Bartels, and S. A. Diddams, "Octave-spanning Ti:sapphire laser with a repetition rate > 1 GHz for optical frequency measurements and comparisons," Opt. Lett. **31**, 1011–1013 (2006).